

Two-dimensional NiTe nanosheets anchored on three-dimensional nickel foam as high-performance catalyst for electrochemical water oxidation

Yibing Li, Chuan Zhao*

School of Chemistry, The University of New South Wales, Sydney, NSW 2052, Australia

*Corresponding author: E-mail: chuan.zhao@unsw.edu.au

Received: 08 February 2017, Revised: 20 March 2017 and Accepted: 9 April 2017

DOI: 10.5185/amlett.2017.1669
www.vbripress.com/aml

Abstract

Development of efficient and affordable electrocatalysts towards water oxidation is important for the large-scale production of hydrogen. Herein, for the first time, we report a two-dimensional (2D) ultrathin NiTe nanosheets as a highly effective catalyst for electrochemical oxygen evolution reaction (OER) via a facile one-pot in-situ hydrothermal approach by using three-dimensional (3D) nickel foam (NF) as both catalyst support and source of nickel. The morphology, electrochemical active surface area (ECSA) and the catalytic activity can be easily engineered by the reaction conditions. The prepared 2D NiTe ultrathin nanosheets have large number of exposed active sites and 3D hierarchical porous structure, which offer superior activity for water oxidation. The electrode only needs an overpotential of 410 mV to afford an extraordinarily high current density of 300 mA cm⁻² and exhibits excellent long-term water catalysis durability. This facile approach for preparation of highly active ultrathin NiTe catalyst is novel and applicable to a wide range of functional materials for various applications including catalysis, energy conversion and energy storage. Copyright © 2017 VBRI Press.

Keywords: NiTe, 2D ultrathin nanosheet, oxygen evolution reaction, electrochemical active surface area (ECSA).

Introduction

Nowadays, global energy crisis and environmental pollution compel us to explore highly efficient and affordable catalysts for clean and sustainable energy generation [1]. Hydrogen has been considered as a clean energy resource to replace the diminishing fossil fuels. In the electrochemical water splitting system which converts electricity into chemical energy in form of hydrogen fuel, the overpotential associated with the oxygen evolution reaction (OER) limits the efficiency of hydrogen production [2-3]. To overcome the large water-splitting overpotential and make the process more energy-efficient, effective oxygen evolution electrocatalysts are thus needed to accelerate the reaction, reduce the overpotential, and enhance the whole energy conversion efficiency.

Currently, scarce and costly RuO₂ and IrO₂ are commonly used as efficient catalysts for OER [4-5]. However, large-scale application of water electrolysis system requires the search of efficient alternative catalysts based on inexpensive and earth abundant elements. Recently, low-cost metal-based oxides [6-7], hydroxides [8-10], sulfides [11], selenides [12] and phosphates [13-

14] etc have been studied and exhibited good electrocatalytic activity for OER in alkaline solution. Especially, transition metal chalcogenides such as metal sulphides and metal selenides materials represent a new family of catalyst materials for water oxidation, due to their unique electronic configuration and comparatively high catalytic activity. NiTe, as a member of metal chalcogenide family and conventionally fabricated in the morphology of nanorods, are regarded as environmentally friendly nanomaterials and used as enzyme mimics to detect glucose and mercury in blood [15-16]. However, its electrochemical activity towards water splitting has never been known to date, to the best of our knowledge. It is shown that good water oxidation catalytic performances have been reported on NiS [11], NiSe [12], CoS [17] and CoSe [18]. Thus, excellent OER performance can be anticipated for NiTe. More importantly, active sites play a key role in catalytic processes. Therefore, exposing more active sites in a catalyst could be an effective way to enhance electrocatalytic performance. Recently, Two-dimensional (2D) materials have emerged as one type of promising electrocatalysts for energy-related reactions. 2D nanosheets with a thickness of a few nanometers or

less can provide a large number of accessible electroactive sites and also decrease the diffusion paths of electrolytes to the material [19-20].

In this study, we report an ultrathin crystalline hexagonal NiTe nanosheet structure grown in-situ from nickel foam (NF) substrates *via* a one-pot hydrothermal method. The electrode can be directly used as a highly efficient, free-standing electrocatalyst for OER in alkaline media. NF is used not only as the catalyst support but also as the source of nickel for the growth of NiTe nanosheets. Moreover, the in-situ fabricated NiTe from NF can facilitate fast electron transfer between the active NiTe composite and the NF charge collector, while the NiTe ultrathin nanosheet provide abundant active sites. Further, the morphology, the electrochemical active surface area (ECSA) and the catalytic activity can be engineered easily by changing the reaction conditions. The non-precious NiTe OER electrode exhibits excellent catalytic activity and durability for water oxidation, demonstrating its promising electrocatalytic applications in water splitting.

Experimental

Material synthesis

The 2D ultrathin NiTe nanosheet was in situ anchored on NF through a facile hydrothermal process. A piece of NF, different amount of Na_2TeO_3 (0.125 mmol, 0.25 mmol and 0.5 mmol) and various amount of hydrazine hydrate (0 mmol, 3 mmol, 7.5 mmol and 15 mmol) dissolved in 10 mL deionized water were put into a Teflon-lined autoclave of 20 mL capacity. After stirring for 10 min, the autoclave was heated at 180 °C for 6 h. After that, the system was allowed to cool to room temperature naturally and the electrode was collected, washed with deionized water and absolute ethanol, and then dried at room temperature.

Physical characterization

Scanning electron microscope (SEM, JSM-7001F) and X-ray diffraction (XRD, Empyrean PANalytical diffractometer, $\text{CuK}\alpha$ radiation) were employed for characterizing the prepared sample. Transmission electron microscopy (TEM), high-resolution TEM (HRTEM), and energy-dispersive X-ray spectroscopy (EDS) mapping images were obtained from Philips CM200. Chemical compositions of the samples were analyzed by X-ray photoelectron spectroscopy (XPS, Thermo ESCALAB250i). Atomic force microscopy (AFM) was carried out on a Dimension ICON SPM scanning probe microscope (Bruker AXS S.A.S.).

Electrochemical measurement

All electrochemical measurements were carried out with a CHI 660 electrochemical workstation. As-prepared NiTe catalyst on NF was directly used as the working electrode without further treatments. A graphite carbon plate and Ag/AgCl (1 M KCl) were used as counter electrode and reference electrode, respectively. All

potentials measured were calibrated to reversible hydrogen electrode (RHE) using the following equation: $E_{\text{RHE}} = E_{\text{Ag}/\text{AgCl}} + 0.235 \text{ V} + 0.059 \text{ pH}$. OER linear sweep voltammetry (LSV) polarization curves were recorded at a scan rate of 5 mV s^{-1} . Before recording, the NiTe electrode was scanned for 20 cycles in 1 M KOH solution from 1.061 V to 1.661 V (*vs.* RHE) until a stable cyclic voltammogram (CV) was recorded. All the OER polarization curves were measured in 1 M KOH with 90% iR compensation. Chronoamperometric measurement was obtained under the same experimental setup without iR compensation. Electrochemical impedance spectra (EIS) of samples were measured at 1.63 V (*vs.* RHE) in the frequency range of 0.1-100,000 Hz with amplitude of 10 mV in 1 M KOH electrolyte.

Calculation of electrochemically active surface area (ECSA)

The calculation of ECSA is based on the measured double layer capacitance (C_{DL}) of the synthesized electrodes in 1 M KOH. Briefly, a potential range where no apparent Faradaic process happened was determined firstly using the static CVs. The charging current i_c which equals to the product of the scan rate (v), and the electrochemical double-layer capacitance, C_{DL} , was measured from the CVs at different scan rates and follows the equation:

$$i_c = v C_{\text{DL}}$$

Thus, the ECSA is positively correlated with the derived curve slope from the equation.

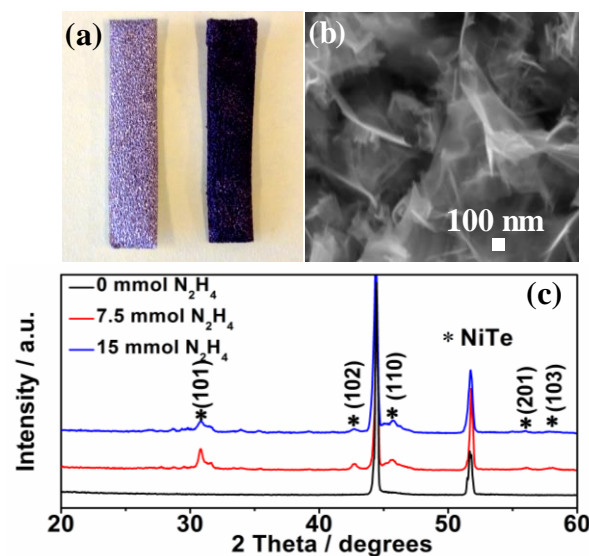
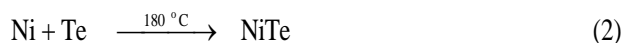
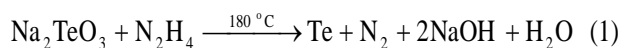


Fig. 1. (a) Photograph of NF (left) and NiTe on NF (right). (b) SEM image of NiTe by using 7.5 mmol N_2H_4 as reductant. (c) XRD spectra of NiTe on NF synthesized with different amount of N_2H_4 .

Results and discussion

The ultrathin NiTe nanosheet was in situ grown from NF through a facile hydrothermal process following the reactions below (Equations 1 & 2):



Firstly, the Na_2TeO_3 , a highly reactive Te source, was sonicated and dissolved into deionized water. Then, different amount of N_2H_4 , which used both as reducing agent and complexing agent to form a uniform and transparent aqueous solution before the reaction, was slowly added into the Na_2TeO_3 solution [21]. Finally, it was heated in the autoclave at 180°C for 6 h where the generated Te from equation (1) and Ni from NF were reacted to form NiTe.

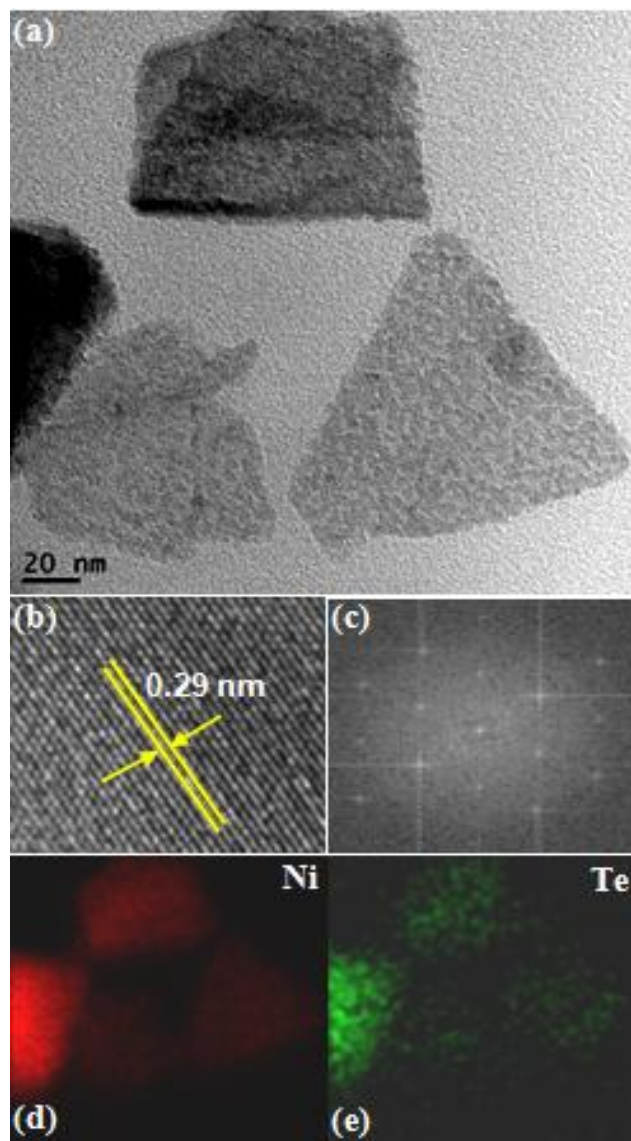


Fig. 2. (a) Low and (b) high magnification TEM images of the ultrathin NiTe nanosheet prepared using 7.5 mmol N_2H_4 as the reducing agent. (c) Fast Fourier transform (FFT) from the area in Fig. 2b. (d) and (e) STEM-EDS elemental mapping of Ni and Te, respectively.

The formation of NiTe can be visually detected from the color change of NF before and after reaction. As shown in **Fig. 1a**, the photograph of bare NF (left) and

NiTe on NF (right) reveals an apparent color change from silver-white to black after the reaction, implying the generation of NiTe. From the scanning electron microscopy (SEM) images of as-obtained product in **Fig. 1b**, ultrathin nanosheets vertically grown on the NF substrate with a length of hundreds of nanometers are observed and the thickness of the nanosheets is only several nanometers. The morphology of the NiTe product can be easily tuned by changing the amount of N_2H_4 . The influence of different N_2H_4 on the morphology of the NiTe was investigated and the results were shown in Fig. S1. The nanosheet morphology can only be obtained when 7.5 mmol N_2H_4 was used. No obvious morphology could be detected in the absence of the N_2H_4 reductant, while densely packed NiTe nanoplates or nanoparticles were gained when treated with less (3 mmol) or more (15 mmol) N_2H_4 . It should be noted that the morphology has a significant influence on the OER, which will be evaluated later.

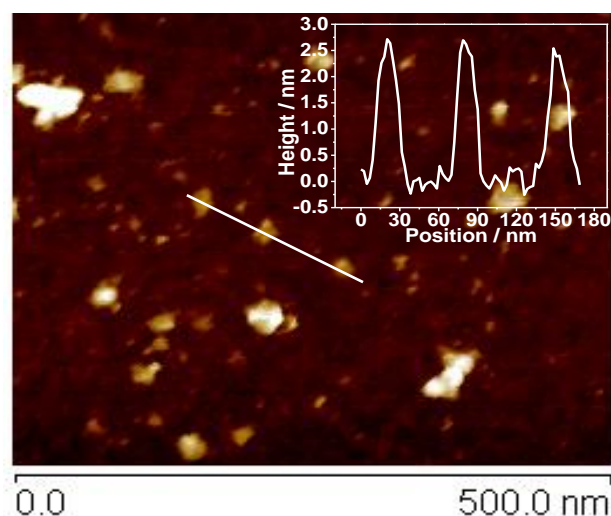


Fig. 3. AFM height image and the corresponding height as a function of position curve (inset) of NiTe in the area indicated by the solid line in the AFM image.

X-ray diffraction analysis (XRD) was used to investigate the crystal structure of NiTe. As shown in **Fig. 1c**, the XRD patterns of various N_2H_4 synthesized samples grown on NF showed peaks of (101), (102), (110), (201) and (103) at 30.9° , 42.8° , 45.7° , 56.2° and 58.2° , respectively, which matched with the hexagonal NiTe phase and peaks at 44.4° and 51.7° arise from the underlying NF substrate. Unsurprisingly, the diffraction peaks of NiTe cannot be detected in the absence of N_2H_4 (0 mmol), which means Na_2TeO_3 could not be reduced to Te without N_2H_4 and therefore, no NiTe was produced.

The morphology of the NiTe ultrathin nanosheet was also characterized by transmission electron microscopy (TEM). As shown in **Fig. 2a**, the TEM image of the product exhibits freestanding sheet-like morphology with relatively low contrast, revealing the ultrathin configuration. Furthermore, the highly parallel and ordered lattice planes in high-resolution TEM (HRTEM) images of NiTe are clearly visible (**Fig. 2b**). The d -spacing of 0.29 nm corresponds to the (101) planes of

hexagonal NiTe crystals. Fast Fourier transform (FFT) performed from the area in Fig. 2b further shows the ultrathin nanosheets have a hexagonal crystal structure (Fig. 2c). Elemental mapping analysis showed that Ni and Te were homogeneously distributed (Fig. 2d and e), and the atomic ratio of Ni/Te is about 1:1, revealing the formed product was single-phase NiTe. The thickness of the ultrathin nanosheet was evaluated further by atomic force microscopy (AFM). The AFM image and its corresponding height profile displayed the sheet-like morphology with an average thickness of approximately 2.5 nm (Fig. 3). Taken together, all of the results confirm that ultrathin 2D NiTe nanosheets have been successfully synthesized.

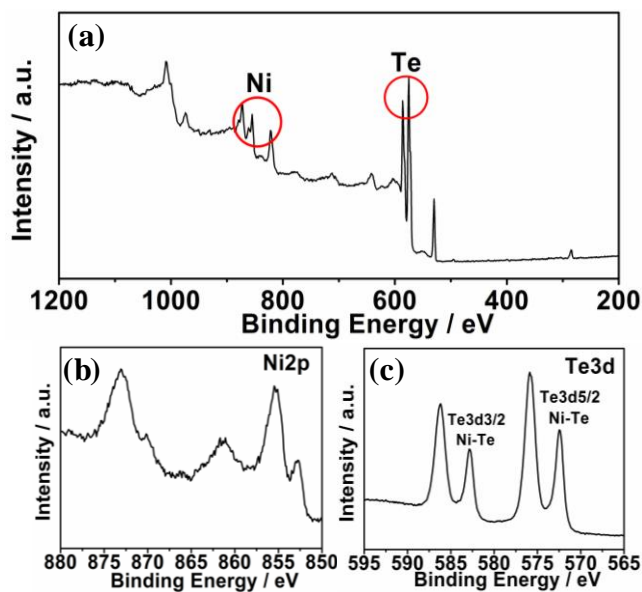


Fig. 4. (a) Survey and high-resolution XPS spectra of (b) Ni2p and (c) Te3d core level regions.

To probe the chemical composition and element valence on the surface of the NiTe electrode, X-ray photoelectron spectroscope (XPS) was performed. The XPS survey spectrum of NiTe on NF clearly shows the characteristic peaks of Ni and Te as shown in Fig. 4a. The high-resolution core spectrum of Ni2p (Fig. 4b) shows Ni2p_{1/2} and Ni2p_{3/2} peaks centered at 873.1 and 855.4 eV with a 6 eV satellite at 861.4 eV, indicating the oxidation state of nickel is Ni²⁺, while the peaks at 852.7 and 870.1 eV can be assigned to metallic Ni2p arising from the NF substrate [14]. The Te3d_{5/2} XPS spectrum of the catalyst gives two peaks at 572.4 and 575.8 eV (Fig. 4c). The higher binding energy at 575.8 eV is due to Te associated with oxygen on the surface and the lower binding energy at 572.4 eV is due to Te bonding to nickel. The Te3d_{3/2} XPS shows peaks at 582.8 and 586.3 eV. Similar to the Te3d_{5/2} XPS spectrum, the lower binding energy at 582.8 eV indicates the nickel telluride bond with a Te⁻² valence in the composite [22]. The atomic composition of the NiTe surfaces determined by the XPS is around 1:1, in consistent with XRD and TEM results, further confirming the formation of NiTe.

The fabricated samples were used as water oxidation catalysts under an alkaline condition. To optimize the OER performance, a set of NiTe electrodes were prepared by changing the amount of Na₂TeO₃ or N₂H₄ precursor in the reaction solution. As shown in Fig. S2a and b, the highest OER performance was obtained for the NiTe electrode prepared with 0.25 mmol Na₂TeO₃ and 7.5 mmol N₂H₄. The less or excess usage of the above reaction precursors result in highly packed nanoplates or nanoparticles structures (Fig. S1). Consequently, lower water oxidation performance was achieved. Furthermore, deliberately adding additional nickel source into the reaction solution NF to prepare NiTe lead to slightly decreased OER performance (Fig. S2c), indicating NF itself can provide sufficient nickel source for the generation of NiTe nanosheet. We also prepared the NiTe powder and loaded it onto NF, however, much worse OER performance was gained (Fig. S2c), demonstrating the in-situ synthetic strategy is vital. Thus, the optimal synthesis condition using 0.25 mmol Na₂TeO₃ and 7.5 mmol N₂H₄ to prepare NiTe on NF was adopted hereafter (denoted as NiTe).

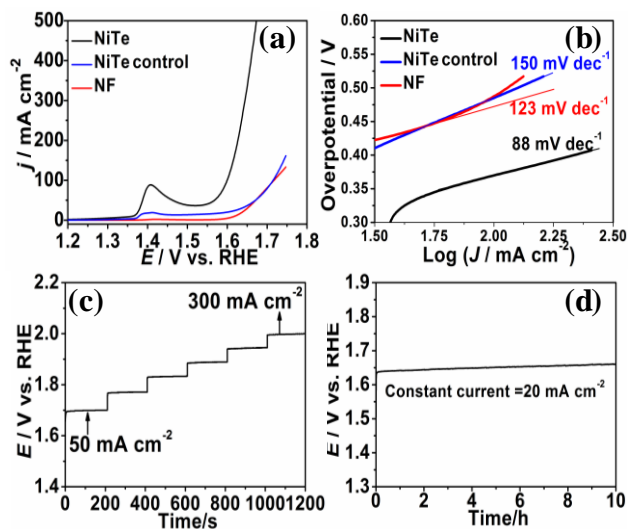


Fig. 5. (a) OER polarization curves of NiTe, NiTe control and NF with 90% *i*R correction and (b) Corresponding Tafel plots. (c) Multi-current chronopotentiometry response for NiTe without *i*R compensation. (d) Chronopotentiometric curve of NiTe electrode with constant current density of 20 mA cm⁻² without *i*R correction.

After optimization, the OER activity of NiTe, NiTe control (prepared without N₂H₄) and NF were compared and investigated under the same condition. As seen from Fig. 5a, bare NF and NiTe control shows negligible OER current, while the polarization curve of NiTe exhibits the lowest onset potential of 1.51 V (*vs.* RHE) and much greater catalytic current density. The overpotential (η) required for delivering a current density of 50 mA cm⁻² is 330 mV, which is even lower than the Ni(OH)₂/NF (372 mV) [23], NiO_x/C (335 mV) [24], NiOOH (525 mV) [25], NiCo₂O₄ (391 mV) [26], Ni/Ni₃N (399 mV) [27] and NiCo LDH (393 mV) [28] electrodes to achieve a current density less than 20 mA cm⁻². Moreover, to deliver a current density as high as 300 mA cm⁻², the overpotential

is only 410 mV. In comparison, only 34 mA cm⁻² and 24 mA cm⁻² can be obtained for NiTe control and NF electrodes, respectively, at the same overpotential. Such catalysts that can achieve large current densities at low overpotentials are highly demanded in water electrolysis industry.

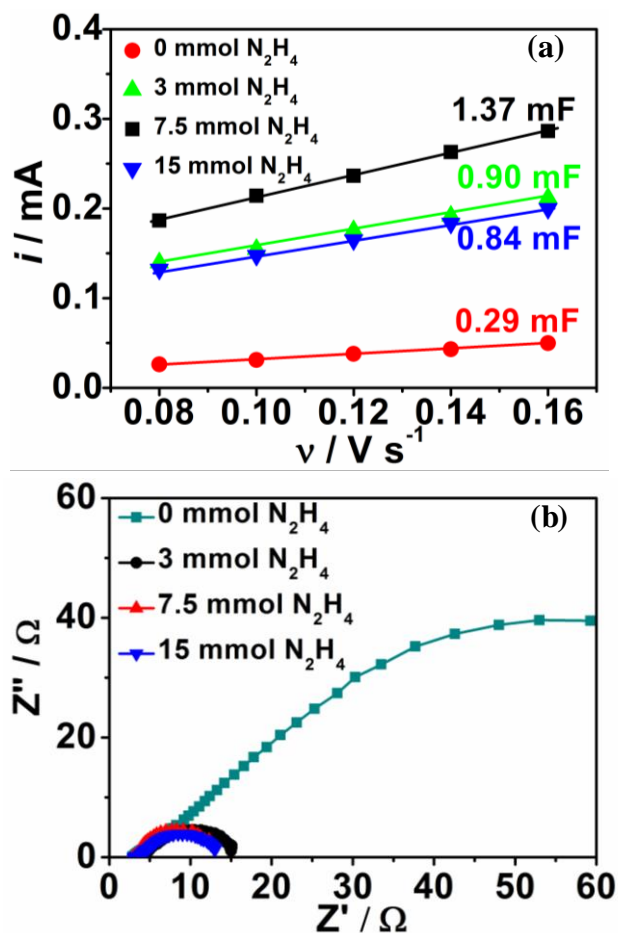


Fig. 6. (a) Comparison of the ECSA sloped measured in a non-Faradaic region and (b) Electrochemical impedance spectra recorded at overpotential of 400 mV (vs. RHE) on different NiTe electrodes.

An important metric for viability of an OER catalyst is its Tafel slope, which could allow for the evaluation of the OER kinetics. As shown in **Fig. 5b**, the Tafel slope for NiTe is 88 mV dec⁻¹, which is much smaller than that of NiTe control (150 mV dec⁻¹) and NF (123 mV dec⁻¹), respectively, indicating rapid OER rates using NiTe electrocatalyst. In addition, the excellent mass transport and charge transfer properties, and robust stability of the NiTe catalyst is evidenced by multi-step chronopotentiometric responses. As seen from **Fig. 5c**, the current density is increased from 50 mA cm⁻² to 300 mA cm⁻² with an increment of 50 mA cm⁻² per 200 s. For each increment, an immediate level off OER potential is observed without detectable fluctuation, demonstrating excellent mass transport and charge transfer, fast bubble removal, and the robustness of the NiTe electrode.

The long-term stability of an electrocatalyst is another crucial parameter to consider for its future practical

applications. As shown in **Fig. 5d**, with continuous OER at a constant current density of 20 mA cm⁻², the overpotential of the NiTe electrode remains stable at around 1.64 V for over 10 h. Furthermore, there is no visible change in morphology for NiTe after the stability test (**Fig. S3**), suggesting the NiTe ultrathin nanosheet is a class of highly active and stable catalyst for the OER.

To understand the origin of the enhanced OER performance of NiTe, we investigated the electrochemical active surface area (ECSA) by determining the double layer capacitance of the different amount N₂H₄ treated samples and the slopes were used to compare their ECSA (**Fig. 6a**). As expected, the NiTe electrode using 7.5 mmol N₂H₄ shows the largest ECSA slope of 1.37 mF, which is around 1.5 times that of 3 mmol and 15 mmol N₂H₄ treated electrodes and 4.7 times that of 0 mmol N₂H₄ fabricated sample, indicating the important role of the 2D ultrathin nanosheet which could expose additional active sites for water oxidation. The enhanced OER activity from the increased ECSA provided by the ultrathin nanosheets could be further confirmed from the electrochemical impedance spectroscopy (EIS) where the charge transfer behavior between the solution and the electrode was evaluated. As seen from **Fig. 6b**, the charge transfer resistance (R_{ct}) of different amount N₂H₄ synthesized NiTe are all around 12 Ω, which are much smaller than the control electrode without using N₂H₄ as reductant. The small R_{ct} of all the prepared NiTe electrodes reveals fast charge transfers during OER between NiTe electrode and the electrolyte, and also implies that higher ECSA provided by the ultrathin nanosheet structure was one of the main factors attributed to the enhanced OER activity.

Conclusion

In conclusion, we have demonstrated a facile in-situ hydrothermal route for the synthesis of hierarchically structured, ultrathin 2D NiTe nanosheet on 3D porous NF substrate. The 2D ultrathin nanosheet together with the 3D configuration of NF can buffer electrolyte to reduce ion transport resistance and facilitate the evolution of O₂. Sample characterizations indicate the higher ECSA provided by the ultrathin nanosheet structure was the main factor for the enhanced OER activity. The resultant NiTe electrode demonstrates excellent OER electrocatalytic activities (an onset potential of 1.51 V vs. RHE and overpotential of 410 mV to afford a high current density of 300 mA cm⁻²). This work may provide a new pathway for the design of advanced OER catalysts.

Acknowledgements

All the physical characterizations were carried out in Mark Wainwright Analytical Centre (MWAC) at the University of New South Wales (UNSW). We thank Dr Bin Gong from MWAC for his assistance in XPS. The study was financed by an ARC Discovery Grant (DP160103107).

Author's contributions

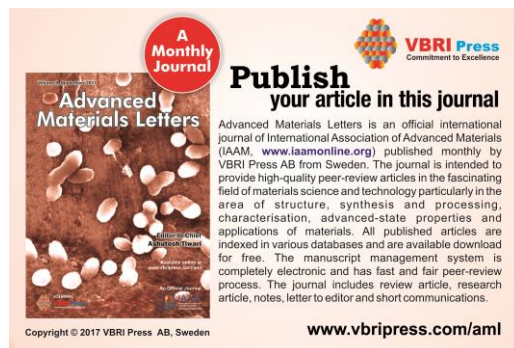
The manuscript was written through contributions of both authors. Both authors have given approval to the final version of the manuscript.

Supporting information

Supporting informations are available from VBRI Press.

References

- Cook, T. R.; Dogutan, D. K.; Reece, S. Y.; Surendranath, Y.; Teets, T. S.; Nocera, D. G. *Chem. Rev.*, **2010**, *110*, 6474.
DOI: [10.1021/cr100246c](https://doi.org/10.1021/cr100246c)
- Chen, S.; Duan, J.; Jaroniec, M.; Qiao, S. Z. *Adv. Mater.*, **2014**, *26*, 2925.
DOI: [10.1002/adma.201305608](https://doi.org/10.1002/adma.201305608)
- Suntivich, J.; May, K. J.; Gasteiger, H. A.; Goodenough, J. B.; Shao-Horn, Y. *Science* **2011**, *334*, 1383.
DOI: [10.1126/science.1212858](https://doi.org/10.1126/science.1212858)
- Sanchez Casalongue, H. G.; Ng, M. L.; Kaya, S.; Friebel, D.; Ogasawara, H.; Nilsson, A. *Angew. Chem. Int. Ed.*, **2014**, *126*, 7297.
DOI: [10.1002/anie.201402311](https://doi.org/10.1002/anie.201402311)
- Walter, M. G.; Warren, E. L.; McKone, J. R.; Boettcher, S. W.; Mi, Q.; Santori, E. A.; Lewis, N. S. *Chem. Rev.*, **2010**, *110*, 6446.
DOI: [10.1021/cr1002326](https://doi.org/10.1021/cr1002326)
- Chen, S.; Duan, J.; Han, W.; Qiao, S. Z. *Chem. Commun.*, **2014**, *50*, 207.
DOI: [10.1039/C3CC47665K](https://doi.org/10.1039/C3CC47665K)
- Xiao, C.; Li, Y.; Lu, X.; Zhao, C. *Adv. Funct. Mater.*, **2016**, *26*, 3515.
DOI: [10.1002/adfm.201505302](https://doi.org/10.1002/adfm.201505302)
- Gong, M.; Li, Y.; Wang, H.; Liang, Y.; Wu, J. Z.; Zhou, J.; Wang, J.; Regier, T.; Wei, F.; Dai, H., *J. Am. Chem. Soc.*, **2013**, *135*, 8452.
DOI: [10.1021/ja4027715](https://doi.org/10.1021/ja4027715)
- Lu, X.; Zhao, C. *Nat. Commun.* **2015**, *6*, 6616.
DOI: [10.1038/ncomms7616](https://doi.org/10.1038/ncomms7616)
- Chen, S.; Duan, J.; Bian, P.; Tang, Y.; Zheng, R.; Qiao, S.-Z. *Adv. Energy Mater.*, **2015**, *5*, 1500936.
DOI: [10.1002/anie.201511447](https://doi.org/10.1002/anie.201511447)
- Feng, L. L.; Yu, G.; Wu, Y.; Li, G. D.; Li, H.; Sun, Y.; Asefa, T.; Chen, W.; Zou, X., *J. Am. Chem. Soc.*, **2015**, *137*, 14023.
DOI: [10.1021/jacs.5b08186](https://doi.org/10.1021/jacs.5b08186)
- Tang, C.; Cheng, N.; Pu, Z.; Xing, W.; Sun, X., *Angew. Chem. Int. Ed.*, **2015**, *54*, 9351.
DOI: [10.1002/anie.201503407](https://doi.org/10.1002/anie.201503407)
- Kanan, M. W.; Surendranath, Y.; Nocera, D. G., *Chem. Soc. Rev.*, **2009**, *38*, 109.
DOI: [10.1039/B802885K](https://doi.org/10.1039/B802885K)
- Li, Y.; Zhao, C., *Chem. Mater.* **2016**, *28*, 5659.
DOI: [10.1021/acs.chemmater.6b01522](https://doi.org/10.1021/acs.chemmater.6b01522)
- Roy, P.; Lin, Z.-H.; Liang, C.-T.; Chang, H.-T., *Chem. Commun.*, **2012**, *48*, 4079.
DOI: [10.1039/C2CC30833A](https://doi.org/10.1039/C2CC30833A)
- Roy, P.; Lin, Z.-H.; Liang, C.-T.; Chang, H.-T., *J. Hazard Mater.*, **2012**, *243*, 286.
DOI: [10.1016/j.jhazmat.2012.10.033](https://doi.org/10.1016/j.jhazmat.2012.10.033)
- Liu, Y.; Xiao, C.; Lyu, M.; Lin, Y.; Cai, W.; Huang, P.; Tong, W.; Zou, Y.; Xie, Y. *Angew. Chem. Int. Ed.*, **2015**, *127*, 11383.
DOI: [10.1002/anie.201505320](https://doi.org/10.1002/anie.201505320)
- Zheng, Y.-R.; Gao, M.-R.; Gao, Q.; Li, H.-H.; Xu, J.; Wu, Z.-Y.; Yu, S.-H., *Small* **2015**, *11*, 182.
DOI: [10.1002/sml.201401423](https://doi.org/10.1002/sml.201401423)
- Bao, J.; Zhang, X.; Fan, B.; Zhang, J.; Zhou, M.; Yang, W.; Hu, X.; Wang, H.; Pan, B.; Xie, Y., *Angew. Chem. Int. Ed.*, **2015**, *54*, 7399-7404.
DOI: [10.1002/anie.201502226](https://doi.org/10.1002/anie.201502226)
- Zhang, X.; Xie, Y., *Chem. Soc. Rev.*, **2013**, *42*, 8187.
DOI: [10.1039/C3CS60138B](https://doi.org/10.1039/C3CS60138B)
- Peng, Q.; Dong, Y.; Li, Y., *Inorg. Chem.*, **2003**, *42*, 2174.
DOI: [10.1021/ic0262031](https://doi.org/10.1021/ic0262031)
- Yao, D.; Liu, Y.; Zhao, W.; Wei, H.; Luo, X.; Wu, Z.; Dong, C.; Zhang, H.; Yang, B., *Nanoscale* **2013**, *5*, 9593.
DOI: [10.1039/C3NR03553K](https://doi.org/10.1039/C3NR03553K)
- Luo, J. S.; Im, J. H.; Mayer, M. T.; Schreier, M.; Nazeeruddin, M. K.; Park, N. G.; Tilley, S. D.; Fan, H. J.; Gratzel, M., *Science* **2014**, *345*, 1593.
DOI: [10.1126/science.1258307](https://doi.org/10.1126/science.1258307)
- Qiu, Y.; Xin, L.; Li, W., *Langmuir* **2014**, *30*, 7893.
DOI: [10.1021/la501246e](https://doi.org/10.1021/la501246e)
- Klaus, S.; Cai, Y.; Louie, M. W.; Trotochaud, L.; Bell, A. T., *J. Phys. Chem. C.*, **2015**, *119*, 7243.
DOI: [10.1021/acs.jpcc.5b00105](https://doi.org/10.1021/acs.jpcc.5b00105)
- Peng, Z.; Jia, D.; Al-Ehizi, A. M.; Elzatahry, A. A.; Zheng, G., *Adv. Energy Mater.*, **2015**, *5*, 1402031.
DOI: [10.1002/aenm.201570050](https://doi.org/10.1002/aenm.201570050)
- Shalom, M.; Ressnig, D.; Yang, X.; Clavel, G.; Fellingner, T. P.; Antonietti, M., *J. Mater. Chem. A* **2015**, *3*, 8171.
DOI: [10.1039/C5TA00078E](https://doi.org/10.1039/C5TA00078E)
- Liang, H.; Meng, F.; Cabán-Acevedo, M.; Li, L.; Forticaux, A.; Xiu, L.; Wang, Z.; Jin, S., *Nano Lett.*, **2015**, *15*, 1421.
DOI: [10.1021/nl504872s](https://doi.org/10.1021/nl504872s)



Advanced Materials Letters
A Monthly Journal

Publish your article in this journal

Advanced Materials Letters is an official international journal of International Association of Advanced Materials (IAAM, www.iaamonline.org) published monthly by VBRI Press AB from Sweden. The journal is intended to provide high-quality peer-review articles in the fascinating field of materials science and technology particularly in the area of structure, synthesis and processing, characterisation, advanced-state properties and applications of materials. All published articles are indexed in various databases and are available download for free. The manuscript management system is completely electronic and has fast and fair peer-review process. The journal includes review article, research article, notes, letter to editor and short communications.

Copyright © 2017 VBRI Press AB, Sweden www.vbripress.com/aml

Supporting information

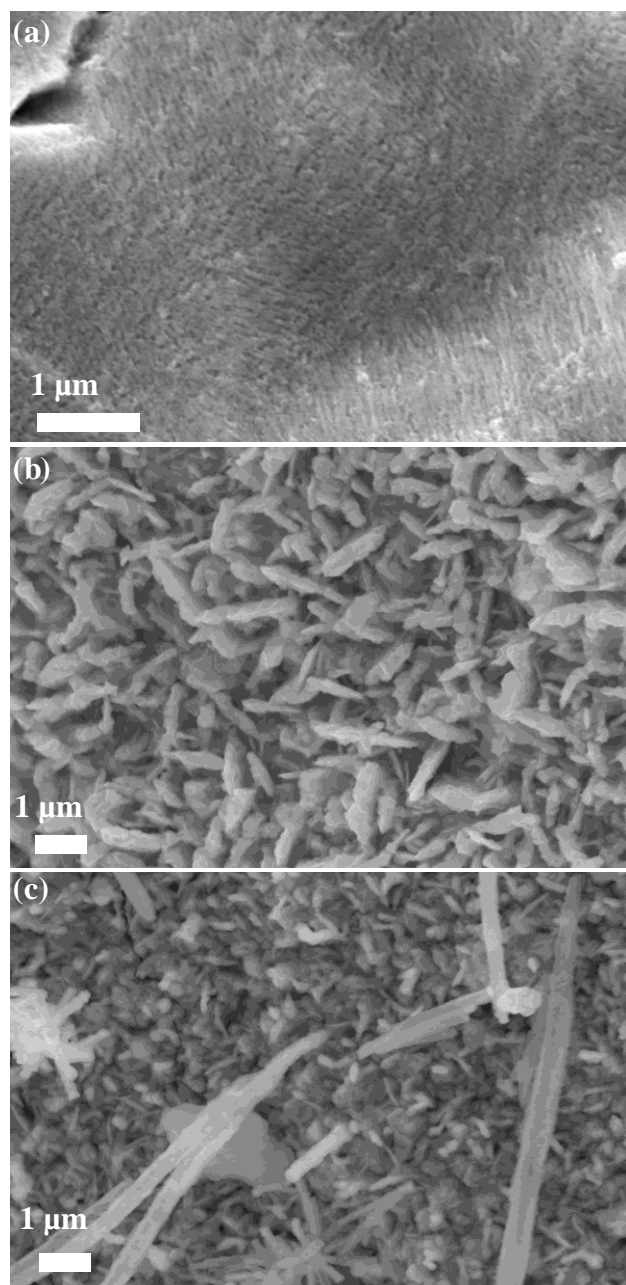


Fig. S1. (a)-(c) SEM image of NiTe synthesized by using 0 mmol, 3 mmol and 15 mmol N_2H_4 as reductant, respectively.

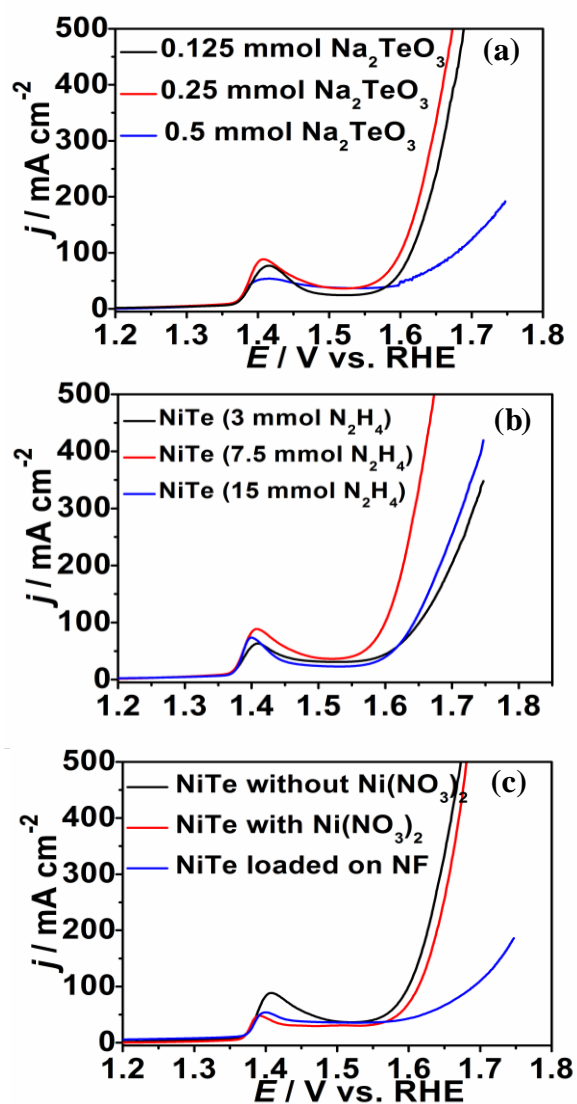


Fig. S2. (a) OER polarization curves of NiTe synthesized by using different Na_2TeO_3 with fixed N_2H_4 (7.5 mmol) and (b) OER polarization curves of NiTe synthesized by using different N_2H_4 with fixed Na_2TeO_3 (0.25 mmol). (c) NiTe electrodes prepared under different conditions.

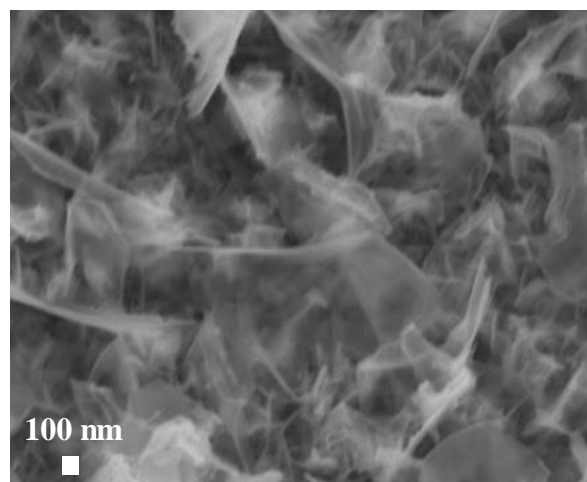


Fig. S3. SEM image of NiTe after stability test.